

Tensor-Valued Time and Inference Path Optimization in Differential Equation-Based Generative Modeling

Dohoon Lee*

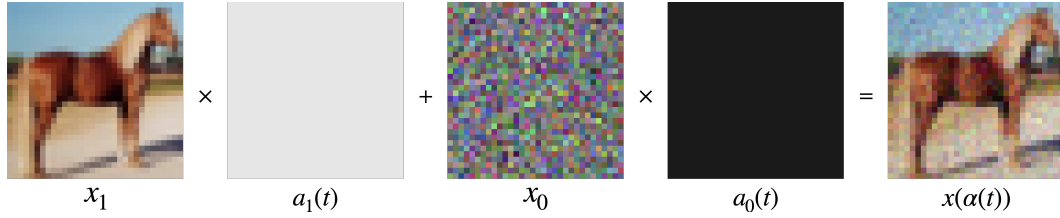
MARG

Seoul National University
ryan0919@snu.ac.kr

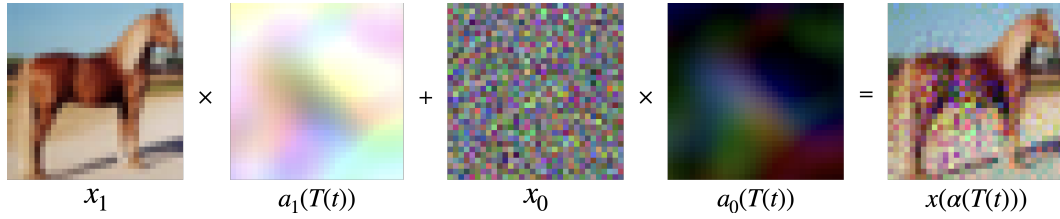
Kyogu Lee

MARG

Seoul National University
kglee@snu.ac.kr



(a) Interpolation with scalar-valued time.



(b) Interpolation with tensor-valued time.

Figure 1: Comparison of interpolation methods in differential equation-based generative modeling.

Abstract

In the field of generative modeling based on differential equations, conventional methods utilize scalar-valued time during both the training and inference phases. This work introduces, for the first time, a tensor-valued time that expands the conventional scalar-valued time into multiple dimensions. Additionally, we propose a novel path optimization problem designed to adaptively determine multidimensional inference trajectories using a predetermined differential equation solver and a fixed number of function evaluations. Our approach leverages the stochastic interpolant framework, simulation dynamics, and adversarial training to optimize the inference pathway. Notably, incorporating tensor-valued time during training improves some models' inference performance, even without path optimization. When the adaptive, multidimensional path derived from our optimization process is employed, further performance gains are achieved despite the fixed solver configurations. The introduction of tensor-valued time not only enhances the efficiency of models but also opens new avenues for exploration in training and inference methodologies, highlighting the potential of adaptive multidimensional paths.

1 Introduction

Differential equation-based generative modeling has become a fundamental approach within the field of generative modeling, demonstrating high effectiveness and facilitating widespread adoption. Research in this domain is primarily divided into two streams: models based on ordinary differential equations (ODEs), which emphasize flow processes [1, 2], and those grounded in stochastic differential equations (SDEs) that focus on diffusion mechanisms [3]. Among these, the study of stochastic interpolants (SI) [4, 5] introduces a framework that effectively bridges the gap between flow and diffusion models. This framework integrates both mechanisms while distinctly separating model training from path design, which are conventionally intertwined processes.

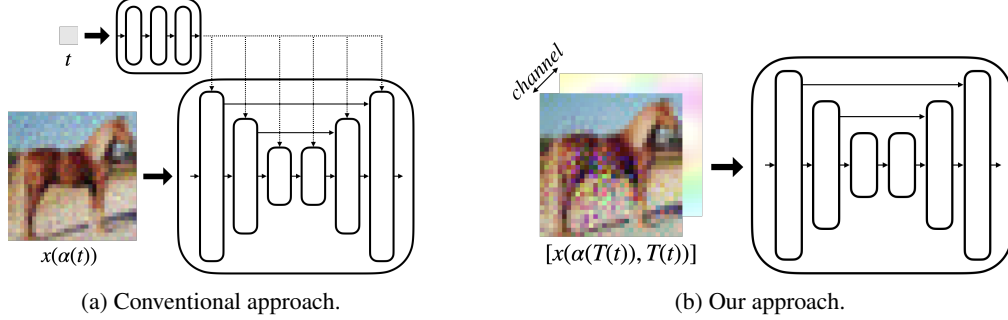


Figure 2: Comparison of input mechanisms in differential equation-based generative modeling.

For the first time in differential equation-based generative modeling, we utilize tensor-valued time, contrasting with the conventional scalar-valued time as shown in Figure 1. For instance, image generation requires learning a mapping function from a Gaussian distribution $x_0 \sim \mathcal{N}(0, I)$ to an image distribution $x_1 \sim \rho_1$, where both x_0 and x_1 are tensors with dimensions $C \times H \times W$ in $\mathbb{R}^{C \times H \times W}$. The interpolant used in training can be described as follows:

$$x(\alpha(t)) = a_0(t)x_0 + a_1(t)x_1, \quad t \in \mathbb{R}. \quad (1)$$

where $\alpha(t) = (a_0(t), a_1(t)) \in \mathbb{R}^2$ represents the interpolation coefficients. Our study introduces tensor-valued time $T(t) \in \mathbb{R}^{C \times H \times W}$, allowing the model to explore interpolation across various dimensions within data distributions. This method broadens the range of data that the model needs to learn and provides detailed information on the interpolation value of each dimension of the data, thereby enhancing its understanding of data distributions by simply replacing t with $T(t)$. Notably, employing tensor-valued time during training decreases some models' Fréchet Inception Distance (FID) [6], even when using simple, unoptimized paths without path optimization.

By incorporating tensor-valued time within the SI framework, we can address a novel question: "Given a differential equation solver operating with a fixed number of function evaluations (NFE), which multidimensional path yields optimal performance when the starting point x_0 is specified?" To explore this, we employ simulation dynamics and an adversarial training approach [7]. This setup includes a neural network g_{θ_0} pre-trained with tensor-valued time, a parameterized path p_{θ_1} , a solver engaged in simulation dynamics, and a discriminator D_{θ_2} evaluating the outcomes to facilitate path optimization. Our experiments demonstrate that multidimensional paths optimized through this methodology significantly decrease FID compared to unoptimized path during inference.

In summary, our **main contributions** are as follows:

1. We are the first to apply tensor-valued time in training differential equation-based generative models, thereby improving performance.
2. By utilizing tensor-valued time, we enable the exploration of multidimensional inference paths, leveraging the increased flexibility it provides in training g_{θ_0} .
3. We introduce a solution for the multidimensional path optimization problem, combining simulation dynamics with adversarial training to find adaptive multidimensional paths for efficient inference.

By employing tensor-valued time, our work broadens the scope of differential equation-based generative modeling and suggests new directions for future research and applications.

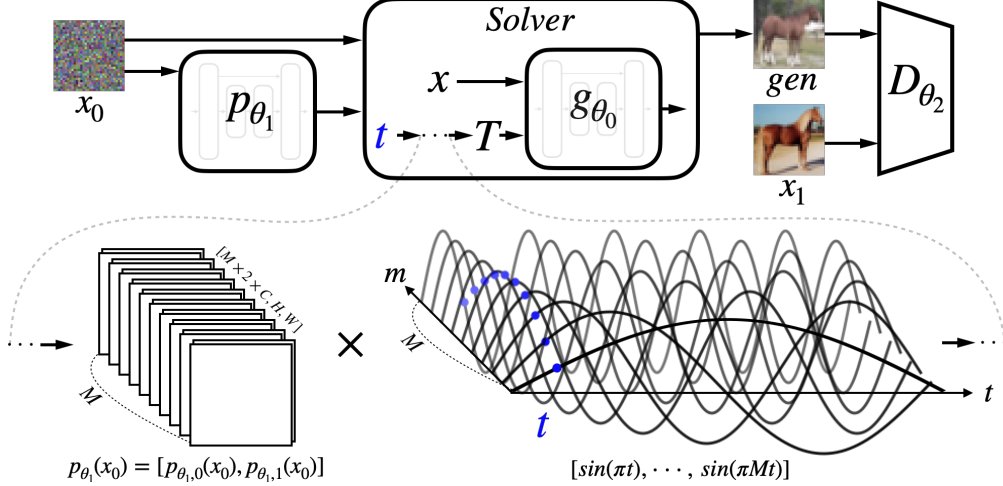


Figure 3: Path optimization process. The path is parameterized via Fourier expansion with Fourier coefficients $p_{\theta_1}(x_0)$. During optimization, g_{θ_0} remains frozen. The solver iteratively computes gen using g_{θ_0} from the initial point x_0 . Subsequently, D_{θ_2} compute the adversarial loss.

2 Related works

Differential equation-based generative modeling Prior to the introduction of diffusion models, continuous normalizing flows (CNFs) [8] were widely adopted in differential equation-based generative modeling. In the training of CNFs, the methodology begins with an initial state x_0 and aims to reach a final state x_1 through simulation dynamics. A distinctive feature of this approach is its direct modeling of the target probability distribution ρ_1 , using likelihood as the direct loss metric. However, this approach is computationally inefficient and underperforms compared to diffusion models. Subsequently, denoising diffusion probabilistic models [9], denoising diffusion implicit models [10], and score-based generative modeling [3], which pre-define a stochastic differential equation (SDE) and train the score or noise value of the SDE using a simulation-free dynamic, demonstrated significant performance improvements. Following the success of score-based diffusion models, ordinary differential equation (ODE)-based methods emerged. Known as flow-based modeling [1, 2], these methods employ CNFs in a simulation-free dynamic similar to diffusion but train vector fields instead of score or noise value, achieving comparable performance. Thus, differential equation-based modeling has been largely divided into ODE-based flow and SDE-based diffusion. Studies such as SF^2M [11] and stochastic interpolant (SI) [4] aim to integrate these methodologies. These frameworks address the transport problem by enabling transitions from any distribution to any other, overcoming the limitations of previous studies confined to Gaussian starting distributions. Notably, SI disentangles the differential equation path design from the training objective, allowing for relatively free path selection without dependencies for training. Later, SI was generalized in a multimarginal setting by Albergo et al. [5], presenting a comprehensive framework for differential equation-based generative modeling.

Path optimizations in differential equation-based generative modeling Path optimizations in differential equation-based generative modeling can be broadly divided into two main directions. First, there is a method of path optimization that defines the pair (x_0, x_1) used in training beforehand, thereby maintaining consistent pairing to straighten the path and improve the model’s inference performance with fewer NFE. For example, Liu et al. [2] identifies pairs through simulation dynamics and retrain the model with these to straighten the path. Additionally, Tong et al. [12] calculates optimal transport pairs on a minibatch basis using the Wasserstein distance for training. Similarly, Goldstein et al. [13] creates coupling by adding noise to x_1 . Secondly, there are methods that define and train models based on their own definitions of the optimal path. Shaul et al. [14] defines optimal paths based on kinetic energy and uses them for model training. Albergo et al. [5] defines optimal paths with the least path length in the Wasserstein-2 metric and conducts path optimization after model training. Although path optimization has been discussed from several perspectives, there has not been a thorough discussion on which multidimensional path to choose in terms of the quality of the generated output when the starting point x_0 is given, while both the solver and the NFE are fixed. In this context, we distinguish our work by addressing such path optimization issues.

3 Preliminaries

Considering a dataset comprised of n samples, $\{x_1^i\}_{i=1}^n \subset \mathbb{R}^{C \times H \times W}$, where each $x_1 \sim \rho_1(x_1)$ and Gaussian $x_0 \sim \mathcal{N}(0, I)$ with $\rho_0(x_0) = \mathcal{N}(0, I)$, generative modeling is the process of transporting distributions from ρ_0 to ρ_1 . We explain three prominent differential equation-based generative modeling approaches: stochastic interpolant (SI), flow, and diffusion.

3.1 Stochastic interpolant

Following Albergo et al. [4], we introduce a stochastic process that interpolates between ρ_0 and ρ_1 .

Definition 1. A stochastic interpolant $x(\alpha(t))$ is defined as:

$$x(\alpha(t)) = a_0(t)x_0 + a_1(t)x_1, \quad (2)$$

where $\alpha(t) = (a_0(t), a_1(t)) \in \mathbb{R}^{2 \times d}$ are differentiable functions with scalar-valued $t \in \mathbb{R}$ within the interval $t \in [0, 1]$, adhering to the conditions $a_0(0) = a_1(1) = 1$ and $a_0(1) = a_1(0) = 0$, ensuring $a_0(t) + a_1(t) = 1$ and $a_0(t), a_1(t) \geq 0$.

$\alpha(t)$ is commonly chosen such that $a_0(t) = 1 - t$ and $a_1(t) = t$. Definition 1 allows the probability distribution of $x(\alpha(t))$ to embody a time-dependent density $\rho(t, x)$, interpolating between $\rho_0(x)$ and $\rho_1(x)$, facilitating generative models through g as follows.

Definition 2. The conditional expectation, represented by g_0 and g_1 , is defined as:

$$g_0(t, x(\alpha(t))) = \mathbb{E}(x_0 | x(\alpha(t))), \quad g_1(t, x(\alpha(t))) = \mathbb{E}(x_1 | x(\alpha(t))) \quad (3)$$

where \mathbb{E} is the expectation over $\rho(x_0, x_1)$ given $x(\alpha(t))$.

For modeling g with the neural network g_θ , it is essential to consider the following theorem.

Theorem 1. The density $\rho(t, x)$ satisfies the transport equation:

$$\partial_t \rho(t, x) + \nabla \cdot (v(t, x) \rho(t, x)) = 0, \quad (4)$$

with the score function when $a_0(t) \neq 0$ and the vector field v :

$$\nabla \log \rho(t, x) = -(a_0(t))^{-1} g_0(t, x), \quad v(t, x) = \dot{a}_0(t) g_0(t, x) + \dot{a}_1(t) g_1(t, x). \quad (5)$$

The g_0 and g_1 uniquely minimize the following objectives:

$$\mathcal{L}_k(\theta) = \int_0^1 \mathbb{E}[|g_{\theta,k}(t, x(\alpha(t)))|^2 - 2x_k \cdot g_{\theta,k}(t, x(\alpha(t)))] dt, \quad k = 0, 1, \quad (6)$$

where the expectation \mathbb{E} is taken over $(x_0, x_1) \sim \rho(x_0, x_1)$.

The vector field v corresponds to the following ordinary differential equation (ODE):

$$\dot{x}_t = v(t, x_t). \quad (7)$$

3.2 Flow and diffusion-based methods

Flow and diffusion define a time-dependent conditional probability path between ρ_0 and ρ_1 as follows:

$$\rho(t, x | x_1) = \mathcal{N}(x | \mu(t, x_1), \sigma(t, x_1)^2 I), \quad x(t) = \mu(t, x_1) + \sigma(t, x_1)x_0. \quad (8)$$

We briefly examine popular methods in flow and diffusion, such as flow matching [1] and denoising diffusion probabilistic models (DDPM) [9].

Flow matching $\mu(t, x_1)$ and $\sigma(t, x_1)$ are defined as follows:

$$\mu(t, x_1) = tx_1, \quad \sigma(t, x_1) = 1 - (1 - \sigma_{\min})t. \quad (9)$$

This conditional probability path produces a vector field $b(t, x | x_1)$ as follows:

$$v(t, x(t) | x_1) = x_1 - (1 - \sigma_{\min})x_0. \quad (10)$$

Flow matching directly models v by a neural network v_θ with the following training objective:

$$\mathcal{L}(\theta) = \mathbb{E}\|v_\theta(t, x(t)) - (x_1 - (1 - \sigma_{\min})x_0)\|^2. \quad (11)$$

DDPM For the standard VP diffusion path, $\mu(t, x_1)$ and $\sigma(t, x_1)$ can be defined as follows:

$$\mu(t, x_1) = \alpha_{1-t}x_1, \quad \sigma(t, x_1) = \sqrt{1 - \alpha_{1-t}^2}, \quad \alpha_t = e^{-\frac{1}{2} \int_0^t \beta(s) ds}, \quad (12)$$

where $\beta(s) = \beta_{\min} + s(\beta_{\max} - \beta_{\min})$, $\beta_{\min} = 0.1$ and $\beta_{\max} = 20$. DDPM models a noise function by a neural network ϵ_θ with the following training objective:

$$\mathcal{L}(\theta) = \mathbb{E} \|\epsilon_\theta(t, x(t)) - x_0\|^2. \quad (13)$$

We can use the following vector field v for ODE-based DDPM inference:

$$v(t, x_t) = -\frac{\beta(1-t)}{2} \left[\frac{\epsilon_t(x)}{\sigma(t, x_1)} - x \right]. \quad (14)$$

Not only SI, flow, and diffusion, but also all the differential equation-based generative models have been defined in scalar-valued time.

4 Tensor-valued time and inference path optimization

We employ tensor-valued time $T(t) \in \mathbb{R}^{C \times H \times W}$ to extend the dimensions of time to match the dimensionality of x_0 and x_1 by replacing t with $T(t)$ in existing differential equation-based generative modeling frameworks. This method is utilized for training g_{θ_0} , b_{θ_0} , and ϵ_{θ_0} as described in Section 3. Additionally, we perform a path optimization process using the stochastic interpolant (SI) framework to identify an adaptive multidimensional path. Path optimization is conducted with g_{θ_0} frozen. The parameterized path p_{θ_1} is conditioned on the initial state x_0 , with both the solver and the number of function evaluations (NFE) fixed. An adversarial training approach, incorporating simulation dynamics, is employed for the optimization process.

4.1 Design choices for tensor-valued time

The spatial range of the tensor-valued time used during the training of g_{θ_0} , b_{θ_0} , and ϵ_{θ_0} not only affects model performance but also impacts the range of paths that can be explored during path optimization. However, a large spatial range can impose a burden on training, potentially degrading performance. Therefore, selecting a tensor-valued time with an appropriate spatial range is crucial. To achieve this, we propose two design strategies:

Example 1. *The Gaussian-noised tensor-valued time (GNT) is described by:*

$$T_{GNT}(t) = \text{clip}(t + s \cdot z, 0, 1), \quad (15)$$

where the function $\text{clip}(x, \min, \max)$ constrains x to the interval $[\min, \max]$. Here, t is a scalar, uniformly distributed as $t \sim \mathcal{U}(0, 1)$. z denotes Gaussian noise, $z \sim \mathcal{N}(0, I)$, with $z \in \mathbb{R}^{C \times H \times W}$. $s \in \mathbb{R}$ is a scale hyperparameter.

This approach is straightforward but does not account for the values between adjacent pixels in images, which are crucial for maintaining the locality of the image. If the scale parameter s is large, it can result in significant differences between adjacent pixel values (Appendix A for more details). To mitigate this, we propose a second design choice constructed as follows:

Example 2. *The low-pass filtered tensor-valued time (LPFT) is described by:*

$$T_{LPFT}(t) = \text{clip}(t + s \cdot f^{LP}(u, G), 0, 1), \quad (16)$$

where $u \in \mathbb{R}^{C \times H' \times W'}$ is sampled from a uniform distribution over the interval $[0, 1]$ as $u \sim \mathcal{U}(0, 1)$ for $H' > H$, $W' > W$. The low-pass filter f^{LP} employs convolution with a Gaussian kernel G , formulated as:

$$f^{LP}(u, G) = 2 \cdot \frac{\text{ECR}(u * G) - \min(\text{ECR}(u * G))}{\max(\text{ECR}(u * G)) - \min(\text{ECR}(u * G))} - 1 \quad (17)$$

Here, the $*$ denotes the convolution operation, ECR denotes edge crop reduction to match the dimension of $u * G$ to $\mathbb{R}^{C \times H \times W}$, and the result of $\text{ECR}(u * G)$ is normalized to the interval $[-1, 1]$. $s \in \mathbb{R}$ is the scale hyperparameter.

We can use the above design choices for tensor-valued time by simply replacing t in differential equation-based generative modeling frameworks with $T(t)$ for training g_{θ_0} , b_{θ_0} , and ϵ_{θ_0} .

4.2 Inference path optimization for adaptive multidimensional path

Path optimization, as depicted in Figure 3, is conducted using the SI framework, simulation dynamics, and adversarial training. Simulation dynamics are performed by iteratively computing the gen using a solver. For simplicity, a first-order Euler solver with $NFE = 10$ is selected as the differential equation solver. Since the Euler solver requires a vector field, we design a parameterized vector field. After simulation, the discriminator receives gen and x_1 and calculates the loss to optimize the path.

Designing a learnable path Following the methodology proposed by Albergo et al. [5], we model the vector field v by the coefficient $\alpha(T_{\theta_1}(t | x_0))$ through a Fourier expansion in t . Our approach deviates from Albergo et al. [5] in two significant aspects: firstly, we use tensor-valued time rather than scalar-valued time, and secondly, we model the multidimensional Fourier coefficients via a neural network $p_{\theta_1}(x_0)$, which depends on $x_0 \sim \rho_0(x_0)$. These modifications allow for the generation of multidimensional paths conditioned on x_0 , thereby facilitating adaptive multidimensional pathfinding.

The parameterized multidimensional coefficients are given by:

$$\alpha(T_{\theta_1}(t | x_0)) = (a_0(T_{\theta_1}(t | x_0)), a_1(T_{\theta_1}(t | x_0))) = (1 - T_{\theta_1}(t | x_0), T_{\theta_1}(t | x_0)). \quad (18)$$

The parameterized tensor-valued time is designed as follows:

$$T_{\theta_1}(t | x_0) = \frac{\tilde{T}_{\theta_1,1}(t | x_0)}{\tilde{T}_{\theta_1,0}(t | x_0) + \tilde{T}_{\theta_1,1}(t | x_0)}, \quad (19)$$

where $\tilde{T}_{\theta_1,0}(t | x_0)$ and $\tilde{T}_{\theta_1,1}(t | x_0)$ are:

$$\begin{aligned} \tilde{T}_{\theta_1,0}(t | x_0) &= 1 - t + \left(\sum_{m=1}^M p_{\theta_1,0,m}(x_0) \cdot \sin(\pi m t) \right)^2, \\ \tilde{T}_{\theta_1,1}(t | x_0) &= t + \left(\sum_{m=1}^M p_{\theta_1,1,m}(x_0) \cdot \sin(\pi m t) \right)^2. \end{aligned} \quad (20)$$

M denotes the Fourier basis count. The neural network p_{θ_1} outputs Fourier coefficients with dimensions $C \times H \times W$, allowing for distinct parameterization of each dimension of the path. Consequently, the parameterized vector field is defined as follows:

$$v_{\theta_0,\theta_1}(t, x | x_0) = \dot{a}_0(T_{\theta_1}(t | x_0)) \cdot g_{\theta_0,0}(T_{\theta_1}(t | x_0), x) + \dot{a}_1(T_{\theta_1}(t | x_0)) \cdot g_{\theta_0,1}(T_{\theta_1}(t | x_0), x). \quad (21)$$

Adversarial training with simulation dynamics We employ v_{θ_0,θ_1} along with a first-order Euler solver to render predictions dynamically through simulation dynamics. Subsequently, both the predictions and x_1 are input to a discriminator for adversarial training [7]. The following is the pseudocode for the path optimization:

Algorithm 1 Path optimization with a first-order Euler solver

```

1: repeat
2:   Sample  $x_0 \sim \mathcal{N}(0, I)$ ,  $x_1 \sim \rho_1(x_1)$ 
3:   Get  $p_{\theta_1}(x_0)$ 
4:   Initialize  $x \leftarrow x_0$ 
5:   for  $n = 0$  to  $N - 1$  do
6:      $t \leftarrow \frac{n}{N}$ 
7:     Calculate  $T_{\theta_1}(t | x_0)$  and  $\dot{\alpha}(T_{\theta_1}(t | x_0))$  using  $p_{\theta_1}(x_0)$ 
8:     Get  $g_{\theta_0}(T_{\theta_1}(t | x_0), x)$ 
9:     Calculate  $v_{\theta_0,\theta_1}(t, x | x_0)$  using  $T_{\theta_1}(t | x_0)$ ,  $\dot{\alpha}(T_{\theta_1}(t | x_0))$ , and  $g_{\theta_0}(T_{\theta_1}(t | x_0), x)$ 
10:    Update  $x \leftarrow x + \frac{1}{N} b_{\theta_0,\theta_1}(t, x | x_0)$ 
11:   end for
12:   Get  $D_{\theta_2}(x)$ ,  $D_{\theta_2}(x_1)$ 
13:   Update parameters  $\theta_1, \theta_2$  using adversarial loss derived from  $D_{\theta_2}(x)$ ,  $D_{\theta_2}(x_1)$ 
14: until convergence

```

Here, N specifies the NFE of solver, and D_{θ_2} represents the discriminator. By freezing parameter θ_0 and optimizing only θ_1 and θ_2 , optimization is focused solely on the path.

Table 1: Comparison of FID \downarrow between scalar-valued time and tensor-valued times ($\text{GNT}_{s=0.005}$ and $\text{LPFT}_{s=0.1}$) for unoptimized paths using the Euler solver. See Appendix C for detailed results.

Method \ NFE	CIFAR-10				ImageNet-32			
	10	100	150	200	10	100	150	200
SI	14.43	4.75	4.51	4.30	17.72	8.08	7.79	7.63
SI_{GNT}	14.59	3.98	3.74	3.63	-	-	-	-
SI_{LPFT}	15.44	3.77	3.68	3.75	17.86	6.63	6.47	6.44
FM	13.70	4.52	4.23	4.07	16.92	7.78	7.53	7.38
FM_{GNT}	13.81	3.59	3.42	3.42	-	-	-	-
FM_{LPFT}	15.13	3.64	3.57	3.64	17.52	6.40	6.27	6.31
DDPM	98.47	6.64	4.84	4.10	111.54	8.13	7.40	7.14
DDPM_{GNT}	105.87	5.40	5.34	7.18	-	-	-	-
$\text{DDPM}_{\text{LPFT}}$	109.08	13.89	23.70	24.26	121.86	11.14	16.83	16.94

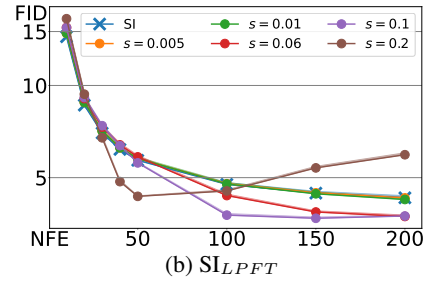
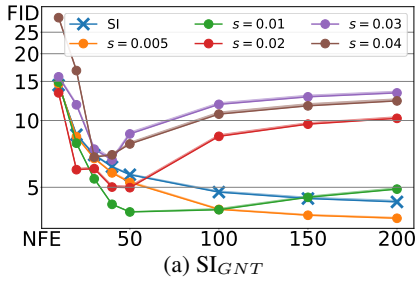


Figure 4: FID for SI with tensor-valued time on CIFAR-10 for an unoptimized path.

5 Experiments

We conduct experiments on the CIFAR-10 [15] and ImageNet at a resolution of 32 [16, 17]. To empirically validate the efficacy of tensor-valued time for various differential equation-based generative modeling approaches, we train g_θ for stochastic interpolant (SI), v_θ for flow matching (FM), and ϵ_θ for denoising diffusion probabilistic models (DDPM) using the design choices for tensor-valued time introduced in Section 4.1. We compare their performance against scalar-valued time. Subsequently, we execute path optimization using SI trained with tensor-valued time, as described in Section 4.2. Since the multidimensional path and the x_0 -conditioned path for path optimization are novel approaches, we conduct experiments to analyze the impact of each element on performance.

5.1 Implementation details

For the configuration of g_θ , v_θ , and ϵ_θ , we use the U-Net architecture proposed by Dhariwal and Nichol [18]. Due to the usage of tensor-valued time, the conventional method of conditioning the time becomes inapplicable. As described in Figure 2, we adopt a straightforward approach by concatenating the tensor-valued time $T(t)$ with the interpolated value $x(\alpha(T(t)))$ along the channel axis, forming an input dimension of $[B, 2C, H, W]$. The output of g_θ consists of $g_{\theta,0}$ and $g_{\theta,1}$, located along the channel axis as described by Albergo et al. [5]. p_{θ_1} uses the U-Net architecture from Ronneberger et al. [19]. As shown in Figure 3, the outputs of p_{θ_1} , namely $p_{\theta_1,0}$ and $p_{\theta_1,1}$, are located along the channel axis. Each $p_{\theta_1,0}$ and $p_{\theta_1,1}$ has a channel shape of $M \times C$, which, through multiplication with M Fourier bases, forms the parameterized multidimensional path. For the LPFT, we basically choose the size of u as $H' = W' = 51$ and the Gaussian kernel G with a size of 18 and $\sigma = 4.0$. All other details are provided in Appendix B.

Table 2: FID of for different σ for the kernel G in $\text{SI}_{\text{LPFT}_{s=0.1}}$ using an Euler solver with an unoptimized path on CIFAR-10.

$\sigma \backslash$ NFE	10	50	100	150	200
0.1	14.89	6.53	9.59	10.67	11.20
1.0	14.92	4.68	6.06	7.01	7.50
2.0	16.25	4.72	3.77	3.95	4.17
4.0	15.44	5.59	3.77	3.68	3.75

Table 3: Path optimization with different inputs to p_{θ_1} for $\text{SI}_{\text{LPFT}_{s=0.1}}$ on CIFAR-10.

Input	1	z	x_0
FID	7.84	6.48	4.14

Table 4: Path optimization with various times for SI on CIFAR-10.

Method	t	$\text{T}_{\text{GNT}}(t)$	$\text{T}_{\text{LPFT}}(t)$
FID	9.75	4.79	4.14

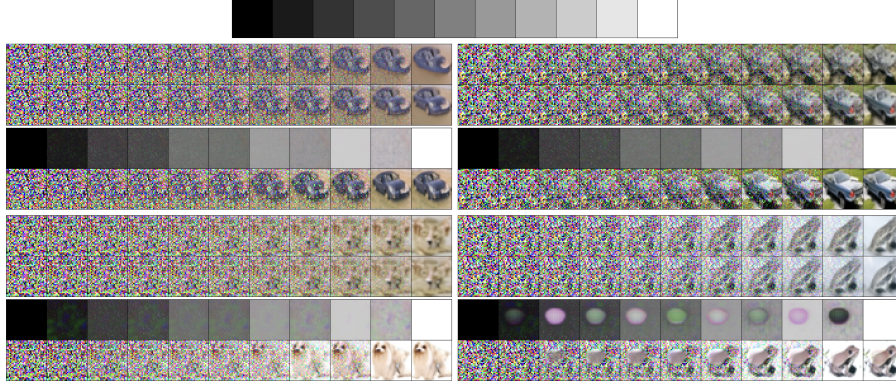


Figure 5: Comparison of results on CIFAR-10: The first and second rows of each example show x_t inferred using SI and $SI_{LPFT_{s=0.1}}$ along an unoptimized path, respectively. The third and fourth rows show $T_{\theta_1}(t | x_0)$ and x_t inferred using $SI_{LPFT_{s=0.1}}$ along an adaptive multidimensional path. The top row displays the unoptimized path for comparison. Additional examples are in Appendix C.

5.2 Results

Impact of tensor-valued time on model performance Table 1 presents the results of using both scalar-valued time and tensor-valued time with an unoptimized path. Interestingly, in SI and FM, most of the FID scores for tensor-valued time are lower compared to those using scalar-valued time. In contrast, for DDPM, scalar-valued time generally yields lower FID scores in most cases. To infer the cause of these results, we can consider the common features between SI and FM compared to DDPM, particularly the vector field underlying training and inference. Both SI and FM use a linear interpolation of x_1 and x_0 with interpolation coefficients t and $1 - t$, respectively. As Lipman et al. [1] noted, this results in a straight vector field. However, DDPM does not maintain the sum of coefficients as 1, and the sum changes with t , resulting in a curved vector field as Lipman et al. [1] showed. Based on these experimental results and analyses, we hypothesize that the effectiveness of tensor-valued time varies depending on how the transport problem between ρ_0 and ρ_1 is modeled.

High-frequency component of tensor-valued time As shown in Figure 4, GNT with $s > 0.01$ does not exhibit a clear trade-off between NFE and FID; instead, an increase in NFE corresponds to higher FID. In contrast, LPFT with $s = 0.1$, even with relatively large scale values compared to GNT, consistently shows a reduction in FID as NFE increases. Additionally, when varying the σ of the Gaussian kernel in LPFT to control high-frequency components (details in Appendix A), the results of training SI_{LPFT} indicate that smaller σ values led to an unclear trade-off between NFE and FID, as shown in Table 2. These results suggest that high-frequency components in tensor-valued time can hinder model training and degrade performance. High-frequency components can cause large differences between adjacent pixel values in the interpolated value $x(\alpha(T(t)))$, reducing the locality characteristics contained in x_1 . Since locality plays a crucial role in the training of convolutional neural networks (CNNs) used to construct U-Net, maintaining the value differences between adjacent pixels within a certain range can help preserve locality, thereby enhancing performance.

Inference with adaptive multidimensional path The FID obtained by performing 10 NFE inference using the adaptive multidimensional paths from path optimization is 4.14 for CIFAR-10 and 7.06 for ImageNet32. This represents approximately a 73% and 60% reduction compared to the FID of 15.44 and 17.86 obtained by performing the same NFE inference using an unoptimized path, as shown in Table 1. These FID values are also lower than those achieved by performing 150 NFE inference using scalar-valued time-trained SI, FM, and DDPM. These results demonstrate that inference using the adaptive multidimensional path obtained from path optimization enables efficient inference. Figure 5 shows examples of adaptive multidimensional paths compared to unoptimized paths. Interestingly, as seen in the bottom right example, p_{θ_1} sometimes shows instances where specific regions are quickly transported.

Impact of x_0 conditioning for path optimization Table 3 shows the effectiveness of using x_0 as an input to p_{θ_1} . The FID is lowest when x_0 is used as the input, compared to using 1 or random Gaussian noise as inputs. Additionally, conditioning on x_0 shows the most stable adversarial training. These empirical evidences suggest that p_{θ_1} extracts relevant information from the ODE’s starting point x_0 to form a path adaptive to x_0 .

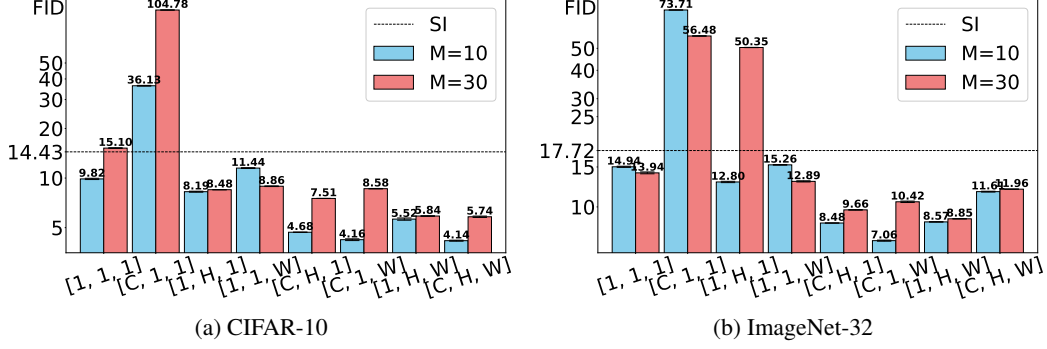


Figure 6: Comparison of FID for paths optimized with different constraints on the output dimension of p_{θ_1} for $M = 10$ and $M = 30$ for $LPFT_{s=0.1}$.

Impact of multidimensionality of path for path optimization To understand the impact of the degree of multidimensionality in the inference path on performance, we conduct various path optimizations by adjusting the expressiveness of p_{θ_1} 's output across channel, width, and height dimensions. This is achieved by taking the mean value across specific dimensions. For example, to maintain multidimensionality in the channel and width but use the same path for the height dimension ([C, 1, W]), we take the mean value only in the height dimension. As shown in Figure 6, utilizing more dimensions generally leads to performance improvements. Adversarial training stability is also better when using more dimensions compared to fewer dimensions. These results suggest that the multidimensionality of adaptive paths can positively influence performance.

Impact of spatial range of tensor-valued time for path optimization To evaluate the impact of the spatial range of tensor-valued time used during SI training on path optimization, we conduct path optimization using SI trained with scalar-valued time, $GNT_{s=0.005}$, and $LPFT_{s=0.1}$. As shown in Table 4, the performance of path optimization improves with an increase in the spatial range of tensor-valued time used during SI training. However, as observed in Figure 4, an excessively large spatial range imposes a burden on SI training. Therefore, when selecting the spatial range of tensor-valued time for path optimization, it is crucial to balance this trade-off and choose an appropriate range.

6 Conclusion

In this study, we depart from the conventional use of scalar-valued time in differential equation-based generative modeling by introducing tensor-valued time. We demonstrate that appropriate design choices for tensor-valued time can enhance model performance. Additionally, we address the novel question of finding x_0 -adaptive multidimensional paths for inference when solver configurations are fixed and x_0 is given. We propose an algorithm that identifies adaptive multidimensional paths using simulation dynamics and adversarial training. Our experimental results show that using an adaptive multidimensional path can reduce the NFE for the solver by approximately 15 times compared to achieving the same performance with unoptimized path. Furthermore, we show the importance of conditioning on x_0 , the multidimensionality of the path, and the spatial range of tensor-valued time for enhancing performance. We anticipate that the introduction of tensor-valued time and adaptive multidimensional paths will pave the way for future research in this field.

Societal Impact Our methods can increase misinformation, create deepfakes, invade privacy, displace jobs, and contribute to environmental issues. Responsible use is essential.

7 Limitations

There are four main limitations in our study. Firstly, our research uses relatively small datasets, making it difficult to generalize our findings. Secondly, we only conduct experiments with the Euler solver. Thirdly, the simulation dynamics used for inference path optimization rely on an iterative inference process with a solver, which is time-consuming and requires substantial VRAM capacity to store gradients at each step. Lastly, adaptive multidimensional paths must use the same solver configuration as during training. While this is not an issue when the inference solver configuration is fixed, it becomes problematic if the configuration changes for each inference.

References

- [1] Yaron Lipman, Ricky T. Q. Chen, Heli Ben-Hamu, Maximilian Nickel, and Matthew Le. Flow matching for generative modeling. In *The Eleventh International Conference on Learning Representations*, 2023. URL <https://openreview.net/forum?id=PqvMRDCJT9t>.
- [2] Xingchao Liu, Chengyue Gong, and qiang liu. Flow straight and fast: Learning to generate and transfer data with rectified flow. In *The Eleventh International Conference on Learning Representations*, 2023. URL <https://openreview.net/forum?id=XVjTT1nw5z>.
- [3] Yang Song, Jascha Sohl-Dickstein, Diederik P Kingma, Abhishek Kumar, Stefano Ermon, and Ben Poole. Score-based generative modeling through stochastic differential equations. In *International Conference on Learning Representations*, 2021. URL <https://openreview.net/forum?id=PxtIG12RRHS>.
- [4] Michael S Albergo, Nicholas M Boffi, and Eric Vanden-Eijnden. Stochastic interpolants: A unifying framework for flows and diffusions. *arXiv preprint arXiv:2303.08797*, 2023.
- [5] Michael Samuel Albergo, Nicholas Matthew Boffi, Michael Lindsey, and Eric Vanden-Eijnden. Multi-marginal generative modeling with stochastic interpolants. In *The Twelfth International Conference on Learning Representations*, 2024. URL <https://openreview.net/forum?id=FHqAzW12wE>.
- [6] Martin Heusel, Hubert Ramsauer, Thomas Unterthiner, Bernhard Nessler, and Sepp Hochreiter. Gans trained by a two time-scale update rule converge to a local nash equilibrium. In I. Guyon, U. Von Luxburg, S. Bengio, H. Wallach, R. Fergus, S. Vishwanathan, and R. Garnett, editors, *Advances in Neural Information Processing Systems*, volume 30. Curran Associates, Inc., 2017. URL https://proceedings.neurips.cc/paper_files/paper/2017/file/8a1d694707eb0fefe65871369074926d-Paper.pdf.
- [7] Ian Goodfellow, Jean Pouget-Abadie, Mehdi Mirza, Bing Xu, David Warde-Farley, Sherjil Ozair, Aaron Courville, and Yoshua Bengio. Generative adversarial nets. In Z. Ghahramani, M. Welling, C. Cortes, N. Lawrence, and K.Q. Weinberger, editors, *Advances in Neural Information Processing Systems*, volume 27. Curran Associates, Inc., 2014. URL https://proceedings.neurips.cc/paper_files/paper/2014/file/5ca3e9b122f61f8f06494c97b1afccf3-Paper.pdf.
- [8] Ricky T. Q. Chen, Yulia Rubanova, Jesse Bettencourt, and David K Duvenaud. Neural ordinary differential equations. In S. Bengio, H. Wallach, H. Larochelle, K. Grauman, N. Cesa-Bianchi, and R. Garnett, editors, *Advances in Neural Information Processing Systems*, volume 31. Curran Associates, Inc., 2018. URL https://proceedings.neurips.cc/paper_files/paper/2018/file/69386f6bb1dfed68692a24c8686939b9-Paper.pdf.
- [9] Jonathan Ho, Ajay Jain, and Pieter Abbeel. Denoising diffusion probabilistic models. In H. Larochelle, M. Ranzato, R. Hadsell, M.F. Balcan, and H. Lin, editors, *Advances in Neural Information Processing Systems*, volume 33, pages 6840–6851. Curran Associates, Inc., 2020. URL https://proceedings.neurips.cc/paper_files/paper/2020/file/4c5bcfec8584af0d967f1ab10179ca4b-Paper.pdf.
- [10] Jiaming Song, Chenlin Meng, and Stefano Ermon. Denoising diffusion implicit models, 2022.
- [11] Alexander Tong, Nikolay Malkin, Kilian FATRAS, Lazar Atanackovic, Yanlei Zhang, Guillaume Hugué, Guy Wolf, and Yoshua Bengio. Simulation-free schrödinger bridges via score and flow matching. In *ICML Workshop on New Frontiers in Learning, Control, and Dynamical Systems*, 2023. URL <https://openreview.net/forum?id=adkj23mvB0>.
- [12] Alexander Tong, Kilian FATRAS, Nikolay Malkin, Guillaume Hugué, Yanlei Zhang, Jarrod Rector-Brooks, Guy Wolf, and Yoshua Bengio. Improving and generalizing flow-based generative models with minibatch optimal transport. *Transactions on Machine Learning Research*, 2024. ISSN 2835-8856. URL <https://openreview.net/forum?id=CD9Snc73AW>. Expert Certification.
- [13] Mark Goldstein, Michael Samuel Albergo, Nicholas Matthew Boffi, Rajesh Ranganath, and Eric Vanden-Eijnden. Stochastic interpolants with data-dependent couplings, 2024. URL <https://openreview.net/forum?id=fK9RkJ4fgo>.
- [14] Neta Shaul, Ricky T. Q. Chen, Maximilian Nickel, Matthew Le, and Yaron Lipman. On kinetic optimal probability paths for generative models. In Andreas Krause, Emma Brunskill, Kyunghyun Cho, Barbara Engelhardt, Sivan Sabato, and Jonathan Scarlett, editors, *Proceedings of the 40th International Conference on Machine Learning*, volume 202 of *Proceedings of Machine Learning Research*, pages 30883–30907. PMLR, 23–29 Jul 2023. URL <https://proceedings.mlr.press/v202/shaul23a.html>.
- [15] Alex Krizhevsky and Geoffrey Hinton. Learning multiple layers of features from tiny images. Technical report, University of Toronto, 2009.

- [16] Patryk Chrabaszcz, Ilya Loshchilov, and Frank Hutter. A downsampled variant of imagenet as an alternative to the cifar datasets. *arXiv preprint arXiv:1707.08819*, 2017.
- [17] Jia Deng, Wei Dong, Richard Socher, Li-Jia Li, Kai Li, and Li Fei-Fei. Imagenet: A large-scale hierarchical image database. In *2009 IEEE conference on computer vision and pattern recognition*, pages 248–255. Ieee, 2009.
- [18] Prafulla Dhariwal and Alexander Nichol. Diffusion models beat gans on image synthesis. In M. Ranzato, A. Beygelzimer, Y. Dauphin, P.S. Liang, and J. Wortman Vaughan, editors, *Advances in Neural Information Processing Systems*, volume 34, pages 8780–8794. Curran Associates, Inc., 2021. URL https://proceedings.neurips.cc/paper_files/paper/2021/file/49ad23d1ec9fa4bd8d77d02681df5cfa-Paper.pdf.
- [19] Olaf Ronneberger, Philipp Fischer, and Thomas Brox. U-net: Convolutional networks for biomedical image segmentation. In *Medical image computing and computer-assisted intervention–MICCAI 2015: 18th international conference, Munich, Germany, October 5-9, 2015, proceedings, part III 18*, pages 234–241. Springer, 2015.
- [20] Maximilian Seitzer. pytorch-fid: FID Score for PyTorch. <https://github.com/mseitzer/pytorch-fid>, August 2020. Version 0.3.0.

Appendices

A Details for tensor-valued time design

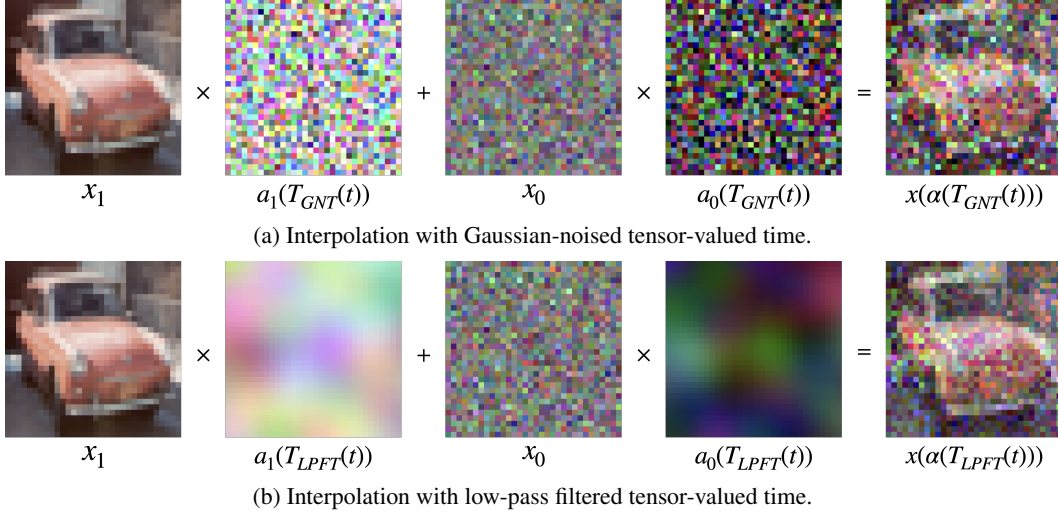


Figure 7: Comparison of interpolation using tensor-valued time with $t = 0.7$ and $s = 0.3$.

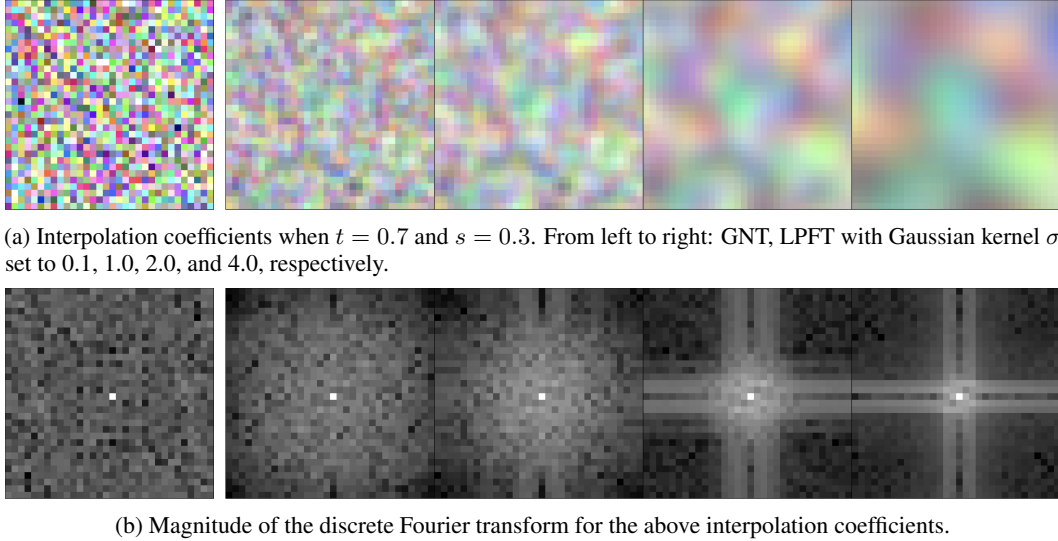


Figure 8: Interpolation coefficients and their discrete Fourier transform magnitudes.

As seen in Figure 7, the interpolated values $x(\alpha(T(t)))$ show differences between Gaussian-noised tensor-valued time (GNT) and low-pass filtered tensor-valued time (LPFT) when using a large scale parameter s . Even with the same s value, LPFT maintains smaller differences between adjacent pixels, whereas GNT exhibits larger differences. This characteristic of LPFT arises because the Gaussian kernel convolution reduces high-frequency components, resulting in a smoothed tensor, as illustrated in Figure 8.

B Implementation details

B.1 Network architectures

Table 5: U-Net configurations for g_θ , v_θ , and ϵ_θ

	CIFAR-10	ImageNet-32
Channels	128	256
Depth	2	3
Channels multiple	1,2,2,2	1,2,2,2
Heads	4	4
Heads Channels	64	64
Attention resolution	16	16
Dropout	0.1	0.1

We use the U-Net architecture from Dhariwal and Nichol [18] for g_θ , v_θ , and ϵ_θ and the U-Net from Ronneberger et al. [19] for p_{θ_1} . For tensor-valued time, we set the existing time embedding part of the U-Net to zero values. Details of the configurations for g_θ , v_θ , and ϵ_θ are provided in Table 5. For p_{θ_1} , we use channel configurations of [256, 512, 1024, 2048]. For D_{θ_2} , we utilize four convolutional layers with 1024 channels, followed by batch normalization and leaky ReLU activation, with a sigmoid activation in the last layer.

B.2 Training configurations

Table 6: Hyper-parameters for training g_θ , v_θ , and ϵ_θ and for path optimization

	CIFAR-10		ImageNet-32	
	Train $g_\theta, v_\theta, \epsilon_\theta$	Path Opt.	Train $g_\theta, v_\theta, \epsilon_\theta$	Path Opt.
Batch size	128	16	512	15
GPUs	1	1	4	1
Iterations	400k	200k	250k	200k
Peak LR	2e-4	2e-4	2e-4	2e-4
LR Scheduler	Poly decay	Poly decay	Poly decay	Poly decay
Warmup steps	5k	5k	5k	5k
Warmup steps for D_{θ_2}	-	20k	-	20k

Our overall training setup is based on the code provided by Tong et al. [11, 12]. Training is conducted on NVIDIA’s RTX 3080Ti or RTX 4090 GPUs. The Adam optimizer with $\beta_1 = 0.9$, $\beta_2 = 0.999$, weight decay of 0.0, and $\epsilon = 1e - 8$ is used along with polynomial decay for learning rate scheduling throughout all training phases. An exponential moving average with a decay rate of 0.999 is also employed during all training phases. For path optimization, we evaluate FID every 10000 steps and report the lowest FID observed. Detailed configurations are provided in Table 6.

B.3 Fréchet inception distance calculation

We employ the PyTorch-FID [20] to compute the Fréchet Inception Distance (FID) using 50,000 generated images. To reduce random variation, generally within $\pm 2\%$, we perform the FID calculation three times for each experiment and report the minimum value.

B.4 Licenses

- CIFAR-10 [15]: MIT license (<https://opensource.org/licenses/MIT>).
- ImageNet [17]: Custom license

C Additional results

Table 7: Comparison of FID between scalar-valued time and various tensor-valued times for differential equation-based generative modeling methods. For a fair comparison, the *modified* version adopts the tensor-valued time’s conditioning approach as detailed in Section 5.1. The scores are computed using an Euler solver with different NFEs.

Method \ NFE	CIFAR-10				ImageNet-32			
	10	100	150	200	10	100	150	200
SI	14.43	4.75	4.51	4.30	17.72	8.08	7.79	7.63
SI _{modified}	14.40	4.77	4.46	4.30	-	-	-	-
SI _{GNT_s=0.005}	14.59	3.98	3.74	3.63	-	-	-	-
SI _{GNT_s=0.02}	13.32	8.48	9.63	10.23	-	-	-	-
SI _{LPFT_s=0.005}	14.80	4.78	4.46	4.30	-	-	-	-
SI _{LPFT_s=0.1}	15.44	3.77	3.68	3.75	17.86	6.63	6.47	6.44
FM	13.70	4.52	4.23	4.07	16.92	7.78	7.53	7.38
FM _{modified}	14.39	4.62	4.30	4.12	-	-	-	-
FM _{GNT_s=0.005}	13.81	3.59	3.42	3.42	-	-	-	-
FM _{GNT_s=0.02}	16.58	4.94	5.68	6.21	-	-	-	-
FM _{LPFT_s=0.005}	14.41	4.63	4.30	4.13	-	-	-	-
FM _{LPFT_s=0.1}	15.13	3.64	3.57	3.64	17.52	6.40	6.27	6.31
DDPM	98.47	6.64	4.84	4.10	111.54	8.13	7.40	7.14
DDPM _{modified}	117.82	10.39	7.20	5.79	-	-	-	-
DDPM _{GNT_s=0.005}	105.87	5.40	5.34	7.18	-	-	-	-
DDPM _{GNT_s=0.02}	102.85	37.13	39.17	40.16	-	-	-	-
DDPM _{LPFT_s=0.005}	113.39	9.47	6.58	5.32	-	-	-	-
DDPM _{LPFT_s=0.1}	109.08	13.89	23.70	24.26	121.86	11.14	16.83	16.94

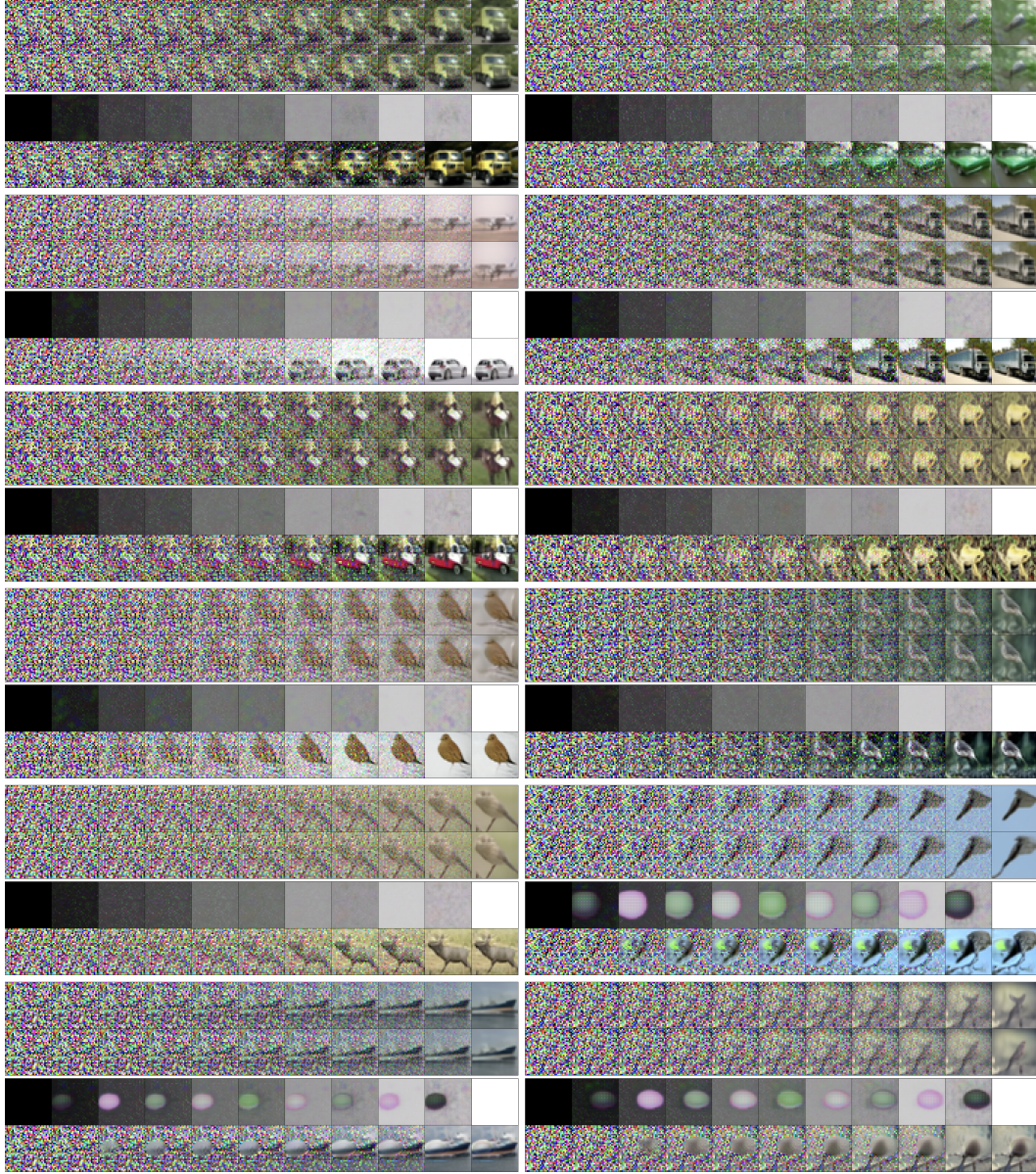


Figure 9: Comparison of results on CIFAR-10: The first and second rows of each example show x_t inferred using SI and $SI_{LPFT_{s=0.1}}$ along an unoptimized path, respectively. The third and fourth rows show $T_{\theta_1}(t | x_0)$ and x_t inferred using $SI_{LPFT_{s=0.1}}$ along an adaptive multidimensional path.



Figure 10: $SI_{LPFT_{s=0.1}}$ with 150 NFE using an unoptimized path on CIFAR-10. FID: 3.68.



Figure 11: $SI_{LPFT_{s=0.1}}$ with 10 NFE using adaptive paths on CIFAR-10. FID: 4.14.

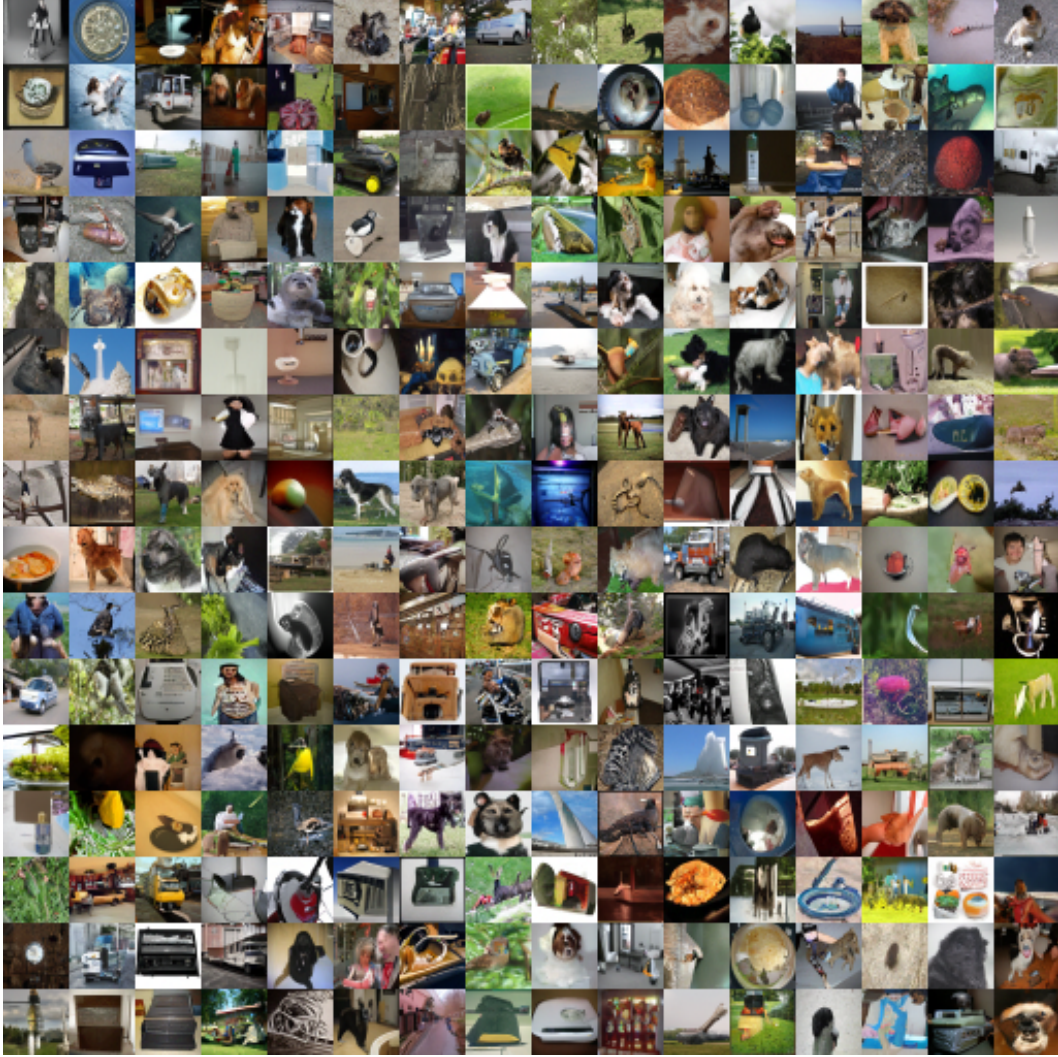


Figure 12: $SI_{LPFT_{s=0.1}}$ with 200 NFE using unoptimized path on ImageNet-32. FID: 6.44



Figure 13: $SI_{LPFT_{\delta=0.1}}$ with 10 NFE using adaptive paths on ImageNet-32. FID: 7.06.